Energy & Environmental Science

ROYAL SOCIETY OF CHEMISTRY

PAPER

View Article Online
View Journal | View Issue

Cite this: *Energy Environ. Sci.*, 2024, **17**, 9335

Data-driven discovery of electrode materials for protonic ceramic cells†

Xueyu Hu,[a] Yucun Zhou,[a] Zheyu Luo,[a] Haoyu Li,[a] Nai Shi,[b] Zhijun Liu,[a] Weilin Zhang,[a] Weining Wang,[a] Yong Ding[a] and Meilin Liu*[a]

Received 21st August 2024,
Accepted 25th October 2024

DOI: 10.1039/d4ee03762f

rsc.li/ees

Protonic ceramic electrochemical cells (PCECs) offer an efficient solution for the closed-loop conversion between chemical and electrical energy, supporting zero-emission objectives. The varying and high-humidity conditions on the oxygen electrode side necessitate the development of novel materials with superior electro-catalytic activity and durability. In this study, we circumvent conventional trial-and-error approaches by utilizing high-throughput calculations and a data-driven decomposition analysis to predict the key properties important for applications of 4455 distinct perovskite oxides, including their thermodynamic stability and decomposition tendencies. Our analysis results in a small number of highly promising candidates. Among them, $PrBaCo_{1.9}Hf_{0.1}O_{5+\delta}$ demonstrates exceptional performance in PCECs, achieving peak power densities of 1.49 W cm^{-2} at 600 °C and 0.6 W cm^{-2} at 450 °C in fuel cell mode and an extraordinary current density (2.78 A cm^{-2}) at an applied voltage of 1.3 V at 600 °C in electrolysis mode, while maintaining outstanding durability over 500 hours of operation. This study highlights the pivotal role of data-driven high-throughput calculations in accelerating the discovery of novel materials for various clean energy technologies.

Broader context

Protonic ceramic electrochemical cells (PCECs) are a critical energy conversion technology with the potential for highly efficient power generation and green hydrogen production, making them vital to achieving a zero-emission society. However, their commercial deployment is hindered by the need for oxygen electrode materials that can operate stably in complex environments while exhibiting high electrocatalytic activity for oxygen reduction and evolution. Accelerating the search for exceptionally active electrode materials, expanding the currently limited understanding, and unraveling their thermodynamic stability and reaction mechanisms remain significant challenges. In this study, we present a research paradigm that integrates high-throughput calculations with a data-driven analysis approach. This paradigm has effectively screened an unprecedentedly vast chemical space, discovering oxygen electrodes that dramatically enhance the kinetics and durability of state-of-the-art PCECs. Our methodology holds promise for advancing the development of various clean energy technologies including other types of fuel cells, solar cells, supercapacitors, and advanced batteries.

Introduction

Amid the urgent challenge of climate change and sustainable development, protonic ceramic electrochemical cells (PCECs) stand out for their exceptional efficiency, affordability, and environmental sustainability, surpassing alternatives like oxygen-ion conducting solid oxide cells (SOCs) and proton exchange membrane electrochemical cells (PEMECs).[1–4] The unique capability of PCECs to seamlessly transition between fuel cell and electrolysis modes at temperatures below 600 °C, coupled with their remarkable conversion efficiency, fosters a sustainable cycle of chemical and electrical energy transformation, paving the way toward a zero-emission future.[5] However, the commercialization of PCECs is hindered by the lack of electro-catalytically active oxygen (or air) electrode materials with excellent resistance to water-induced element segregation, phase transformation, and delamination, particularly when exposed to high concentrations of steam in the electrolysis mode.[6] Various strategies have been employed to address these problems, including surface infiltration, pulsed laser deposition (PLD) assisted interlayer construction, and acid etch triggered interface enhancement.[3,7,8] However, their complexity greatly increases the cost, thus diminishing their

[a] *School of Materials Science and Engineering, Georgia Institute of Technology, Atlanta, 30332-0245, USA. E-mail: meilin.liu@mse.gatech.edu*
[b] *Kyushu University Platform of Inter-/Transdisciplinary Energy Research, Kyushu University, Fukuoka, 819-0395, Japan*

† Electronic supplementary information (ESI) available: Supplementary notes, figures, and tables. See DOI: https://doi.org/10.1039/d4ee03762f

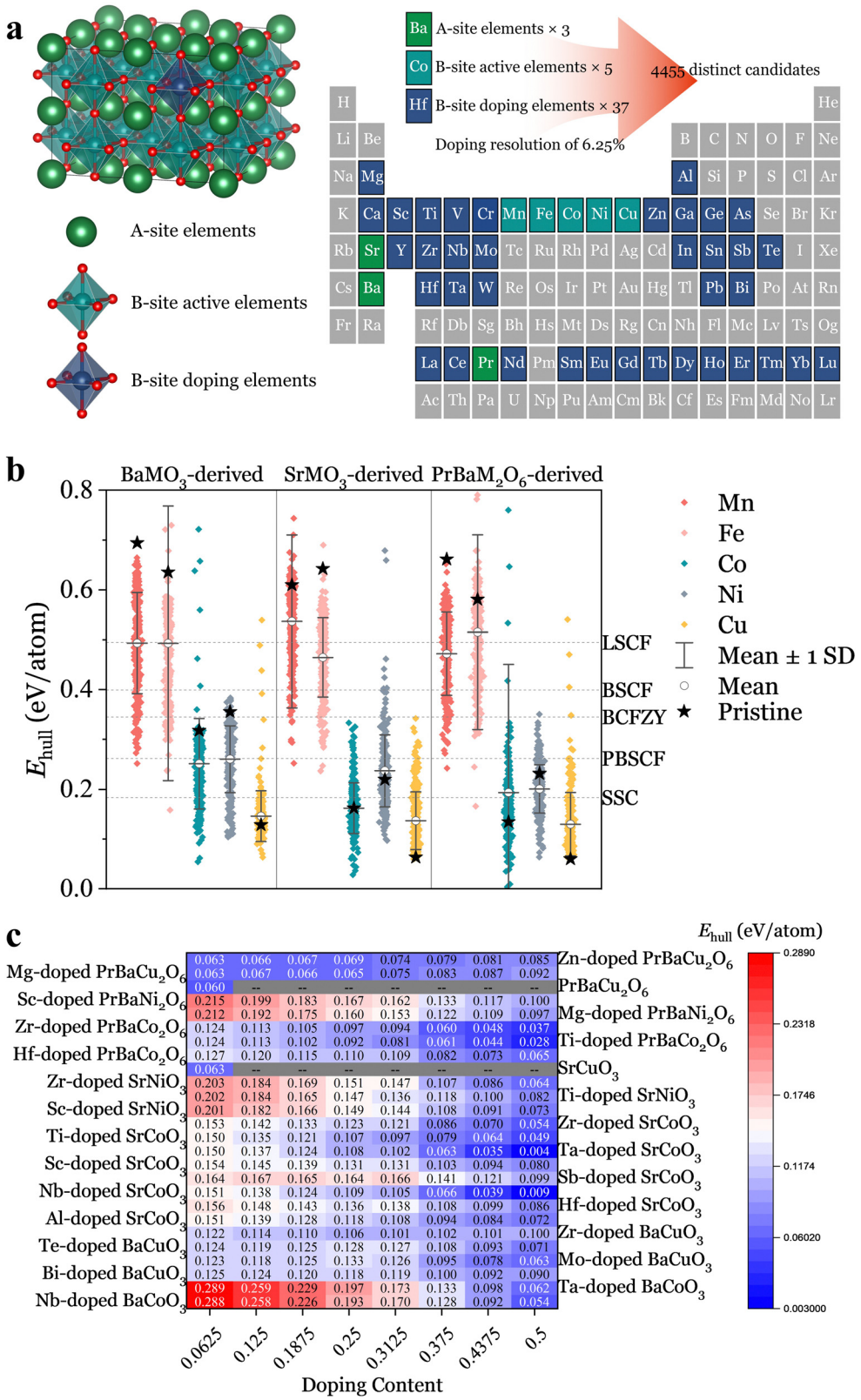

Fig. 1 Accelerated screening of materials *via* high-throughput DFT calculation for thermodynamic stability. (a) Depiction of the bulk structures for perovskite candidates with dimensions of $2\sqrt{2}a \times 2\sqrt{2}a \times 2a$, and illustration of the chosen elements from the periodic table for constructing perovskite candidates. (b) E_{hull} values for the perovskite candidates, organized into 15 groups based on variations in A-site and B-site active elements. The mean value and standard deviation are indicated for each group. Additionally, E_{hull} values for both pristine and state-of-the-art materials are provided for benchmarking purposes. (c) Promising perovskite candidates showcasing exceptional thermodynamic stability, detailed for 26 series materials.

commercial applicability. This underscores an urgent need for the development of inherently durable oxygen electrode materials.

To bypass conventional, time-consuming methods for material discovery, we are leveraging high-throughput density functional theory (DFT) calculations.[9–12] These calculations enable precise material characterization and broaden the horizons of chemical exploration, shifting the paradigm from intuition-based to data-driven material selection.[13–16] Incorporating the thermodynamic stability descriptor, E_{hull}, these techniques offer remarkable efficiency in evaluating the thermodynamic stability of new materials without the need for experimental synthesis.[10,17,18] However, relying excessively on E_{hull} values alone risks overlooking potential decomposition tendencies, which could potentially skew assessments of materials' stability. To address this, we propose a data-driven material analysis method termed the decomposition analysis (DA), based on the expanding landscape of open-access databases,[19] that assesses stability more accurately by examining the stable phases constructing a material's convex hull. Our study applied high-throughput DFT calculations across an unprecedented size of 4455 oxygen electrode candidates, identifying 26 material series with outstanding thermodynamic stability. Further refinement through DA and experimental validation led to the discovery of a highly durable composite oxygen electrode, $PrBaCo_{1.9}Hf_{0.1}O_{5+\delta}$ (PBCHf10), which exhibits exceptionally high electro-catalytic activity. Our integrated approach, combining experimental validation with advanced computational methods, has unraveled the mechanism of the proton-involved oxygen reduction reaction, potentially setting a new theoretical benchmark for the development of PCEC oxygen electrodes. A PCEC based on the PBCHf10 electrode demonstrates outstanding performance, achieving an impressive peak power density (1.49 W cm^{-2}) in the fuel cell mode and an extraordinary current density (2.78 A cm^{-2}) at an applied cell voltage of 1.3 V in the electrolysis mode at 600 °C. Notably, the single cell maintains stable performance for over 500 hours in the electrolysis mode.

Results and discussion

Unveiling unexplored chemical spaces *via* high-throughput calculations

Drawing inspiration from the state-of-the-art oxygen electrode materials, such as $La_{0.6}Sr_{0.4}Co_{0.2}Fe_{0.8}O_{3-\delta}$ (LSCF),[20] $Ba_{0.5}Sr_{0.5}Co_{0.8}Fe_{0.2}O_{3-\delta}$ (BSCF),[21] $Sm_{0.5}Sr_{0.5}CoO_{3-\delta}$ (SSC),[22] $BaCo_{0.4}Fe_{0.4}Zr_{0.1}Y_{0.1}O_{3-\delta}$ (BCFZY),[23] and $PrBa_{0.5}Sr_{0.5}Co_{1.5}Fe_{0.5}O_{5+\delta}$ (PBSCF),[24] we explored previously uncharted chemical spaces. We constructed a comprehensive set of perovskite oxide candidates by selecting three A-site ions (Ba, Sr, $Pr_{0.5}Ba_{0.5}$) and combining them with five catalytically active B-site ions (Mn, Fe, Co, Ni, Cu) plus 37 distinct B-site dopants (Table. S1, ESI†). To ensure sufficient electro-catalytic activity, the proportion of the catalytically active B-site ions was kept above 50%. This approach generates 4455 distinct perovskite oxide candidates, 96% of which were previously unexplored, as showcased in Fig. 1a. The optimal elemental distribution for each candidate was determined using molecular dynamics–Monte Carlo (MD–MC) simulations.[25,26] We performed structural relaxation and static calculations to derive their E_{hull} values under oxygen electrode operation conditions (T = 600 °C, $p(O_2)$ = 0.21 atm), a crucial descriptor of thermodynamic stability. This descriptor acts as a metric to determine the likelihood of a material undergoing phase transformation or decomposition into a mixture of more stable phases on the convex hull.[26]

We organized the E_{hull} values for the 4455 materials into three main categories based on A-site elements, further classifying them by B-site active elements, resulting in 15 distinct groups (Fig. 1b). The pristine perovskite oxides in each group are highlighted, and we present their mean E_{hull} values along with standard deviations. From the analysis of these preliminary data, those with Mn and Fe at the B-site, exhibit relatively high E_{hull} values, with averages ranging from 0.465 to 0.537 eV per atom, suggesting their inherent instability. The lowest E_{hull} value is observed with $BaFe_{0.5}Mo_{0.5}O_3$, sacrificing 50% active elements to achieve a value of 0.158 eV per atom, which is still not satisfactory (Fig. S1 and S2, ESI†). In contrast, materials with Co or Ni at the B-site demonstrate lower E_{hull} values, with averages ranging from 0.164 to 0.260 eV per atom, indicating better stability (Fig. S3 and S4, ESI†). Pristine oxides with Cu at the B-site demonstrate the lowest E_{hull} values, at 0.129, 0.063, and 0.060 eV per atom for $BaCuO_3$, $SrCuO_3$, and $PrBaCu_2O_6$, respectively. However, subsequent doping efforts typically result in elevated E_{hull} values (Fig. S5, ESI†).

Fig. 1c summarizes the top 26 series materials, highlighting them as the most stable and promising candidates for potential applications. Furthermore, a comparative analysis of the state-of-the-art oxygen electrodes was performed to contextualize the thermodynamic stability of our materials, with their E_{hull} values denoted in Fig. 1b for a direct comparison. Among them, SSC exhibited the lowest E_{hull} value of 0.183 eV per atom, yet it still falls short of the optimal series materials outlined in Fig. 1c. Notably, several materials highlighted in Fig. 1c, including $BaCo_{0.8}Ta_{0.2}O_{3-\delta}$,[27] $SrCo_{0.8}Nb_{0.1}Ta_{0.1}O_{3-\delta}$,[28] $SrCo_{0.8125}Sb_{0.1875}O_{3-\delta}$,[29] $SrCo_{0.8}Sc_{0.175}Nb_{0.025}O_{3-\delta}$,[30] and $PrBaCo_{1.92}Zr_{0.08}O_{5+\delta}$,[31] have already been successfully used as oxygen electrodes, demonstrating robust stability against various environmental conditions. It is worth noting that the development of these materials was initially serendipitous and lacked a systematic approach. However, the integration of high-throughput calculations and methodical screening has streamlined their discovery and optimization.

Data-driven enhanced insight into the thermodynamic stability

Despite the widespread application of the E_{hull} theory, we emphasize the critical importance of not neglecting the formation energy (E_F) of the stable phases constituting the convex hull for the materials under investigation. This oversight can lead to a failure to identify potential decomposition tendencies, resulting in inaccuracies in evaluating the thermodynamic stability. In response to this limitation and to enhance the practicality of our computational insights across all 4455 materials, we

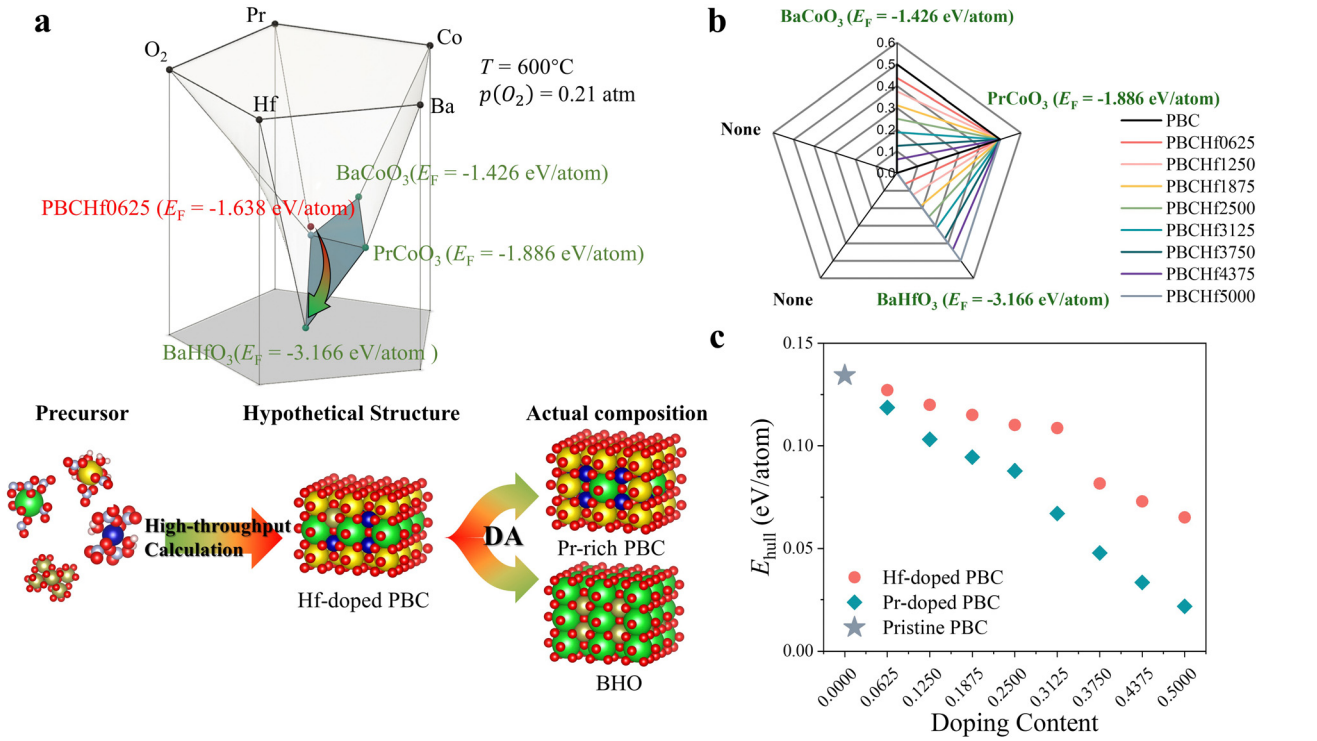

Fig. 2 Decomposition analysis method. (a) Three-dimensional depiction of the convex hull underlying the material PBCHf0625, along with an illustration of the objective of decomposition analysis. (b) Two-dimensional representations of the decomposition analysis for Hf-doped PBC series materials. (c) Direct comparison of Hf-doped and Pr-doped PBC, using pristine PBC as a reference.

have introduced an innovative material analysis method named decomposition analysis (DA) (Fig. S6, ESI†). This method delineates the convex hull underlying a material and provides an exhaustive array of potential decomposition pathways, utilizing data from the Materials Project.[19] For example, the convex hull underlying $PrBaCo_{1.875}Hf_{0.125}O_6$ (PBCHf0625), one of the $PrBaCo_2O_6$-derived materials, should be formed by up to five stable materials as a quinary oxide. This five-dimension phase diagram is visually illustrated in Fig. 2a, which depicts the three-dimensional convex hull underlying PBCHf0625. Through this representation, we identified three stable materials – $BaCoO_3$, $PrCoO_3$, and $BaHfO_3$ – as the constituents of the convex hull. Notably, the significant disparity in E_F between PBCHf0625 (−1.638 eV per atom) and $BHfO_3$ (−3.166 eV per atom) underscores a pronounced tendency of PBCHf0625 to decompose and lead to the formation of $BaHfO_3$, a critical fact that is obfuscated by its deceptively low E_{hull} value (0.127 eV per atom). This theoretical prediction was substantiated through empirical experiments (Fig. S7, ESI†). For a more intuitive understanding, Fig. S8 (ESI†) offers a simplified two-dimensional projection of Fig. 2a, clearly indicating the E_F of PBCHf0625 alongside the three potential decomposition products.

The efficacy of DA is unequivocally proven through its successful application to well-known oxygen electrode materials and its precision in discerning subtle differences among a variety of PBC-derived materials (detailed in supplementary notes and Fig. S9–S12, ESI†). Subsequently, DA was applied to all 4455 materials to provide a comprehensive assessment of potential decomposition products. This approach leverages over 30 000 diverse materials, representing a fifth of the entire Materials Project database, offering invaluable data-driven insights into their thermodynamic stability. As we reexamined the optimal perovskite oxides featuring the greatest thermodynamic stability listed in Fig. 1d, our analysis highlighted Hf, Ti, and Zr-doped PBC series materials. These materials, derived from an established oxygen electrode PBC, consistently demonstrate lower E_{hull} values across various doping contents, marking them as notably superior compared to other candidates. The DA method further highlights the complex decomposition behavior of Ti and Zr-doped PBC series materials, as detailed in Table S2 (ESI†), distinguishing them from the Hf-doped ones. As illustrated in Fig. 2b, the Hf-doped $PrBaCo_2O_6$ series consistently manifests one primary decomposition product – $BaHfO_3$ – across various doping contents. Initially denoted as $PrBaCo_{2-x}Hf_xO_6$, the Hf-doped $PrBaCo_2O_6$ series inherently comprises two distinct phases: $PrBa_{1-x}Co_{2-x}O_{6-3x}$ (Pr-rich PBC) and $BaHfO_3$. Given that $BaHfO_3$ is located on the convex hull, indicating optimal stability, our focus intensifies on the Pr-rich PBC, the major phase within this composite. As demonstrated in Fig. 2c, replacing Ba with Pr incrementally lowers the E_{hull} values with an increasing doping content, suggesting further enhanced thermodynamic stability compared with Hf-doped PBC. Notably, the minimum value is achieved with $PrCoO_3$, standing at 0.022 eV per atom. Even expanding our investigation beyond merely Pr-rich PBC to $PrBaCo_2O_6$-derived materials, which undergo Ba-site substitution with 23 different dopants resulting in 184 distinct materials, Pr-rich PBC

consistently exhibits the lowest E_{hull} values, as shown in Fig. S13 (ESI†). Ultimately, integrating the E_{hull} theory with the DA method has provided comprehensive insights into the thermodynamic stability of Hf-doped $PrBaCo_2O_6$ series materials. Characterized by Pr-rich PBC alongside $BaHfO_3$, these composite materials demonstrate excellent thermodynamic stability among all 4455 distinct candidates.

Structural verification

The experimental assessment focuses on the Hf-doped PBC series materials (PBCHf), employing a methodical approach of decimal substitution to synthesize $PrBaCo_{2-x}Hf_xO_{5+\delta}$ (where x = 0, 0.05, 0.1, 0.15 and 0.2, respectively labeled as PBC, PBCHf05, PBCHf10, PBCHf15, and PBCHf20). The XRD patterns shown in Fig. 3a indicate that the pristine PBC exhibits a double perovskite structure. The substitution of Co with Hf on the B-site leads to the emergence of a secondary phase, marked by a new peak at $2\theta = 30.65^\circ$. The intensity of the peak corresponding to the secondary phase increases proportionally with the Hf content, suggesting a compositional dependency. Evidence from DA of PBCHf, as represented in Fig. 2b, suggests that the primary phase corresponds to Pr-rich PBC, while the secondary phase is identified as BHO. It is worth noting that upon reaching a doping content of x = 0.2, the primary phase transforms from a double to a simple perovskite structure, as evidenced by the absence of peak splitting for the (110), (211), (220), and (310) planes. This phenomenon is likely attributable to the increased Pr/Ba ratio. Rietveld refinement analysis of PBCHf10, depicted in Fig. S14 (ESI†), confirmed that the major phase, Pr-rich PBC, has a space group $P4/mmm$ with lattice parameters of a = 3.90 Å and c = 7.65 Å. The secondary phase, BHO, corresponds to the space group $Pm\bar{3}m$ with the lattice parameter a = 4.17 Å. High-resolution transmission electron microscopy (HRTEM) and energy-dispersive X-ray spectroscopy (EDS) further support the phase composition predicted by the DA method. As depicted in Fig. 3b, EDS mapping of a larger particle (area 1) reveals homogeneous distribution of Pr, Ba, Co, and O with Pr-excessive characteristics, attributed to the Pr-rich PBC. The smaller particle (area 2), in contrast, consists exclusively of Ba, Hf, and O with an equimolar ratio of Ba to Hf, consistent with the characteristics of the BHO phase. Further insights are gleaned from the selected area electron diffraction (SAED) pattern (Fig. 3c), focusing on the larger particle.

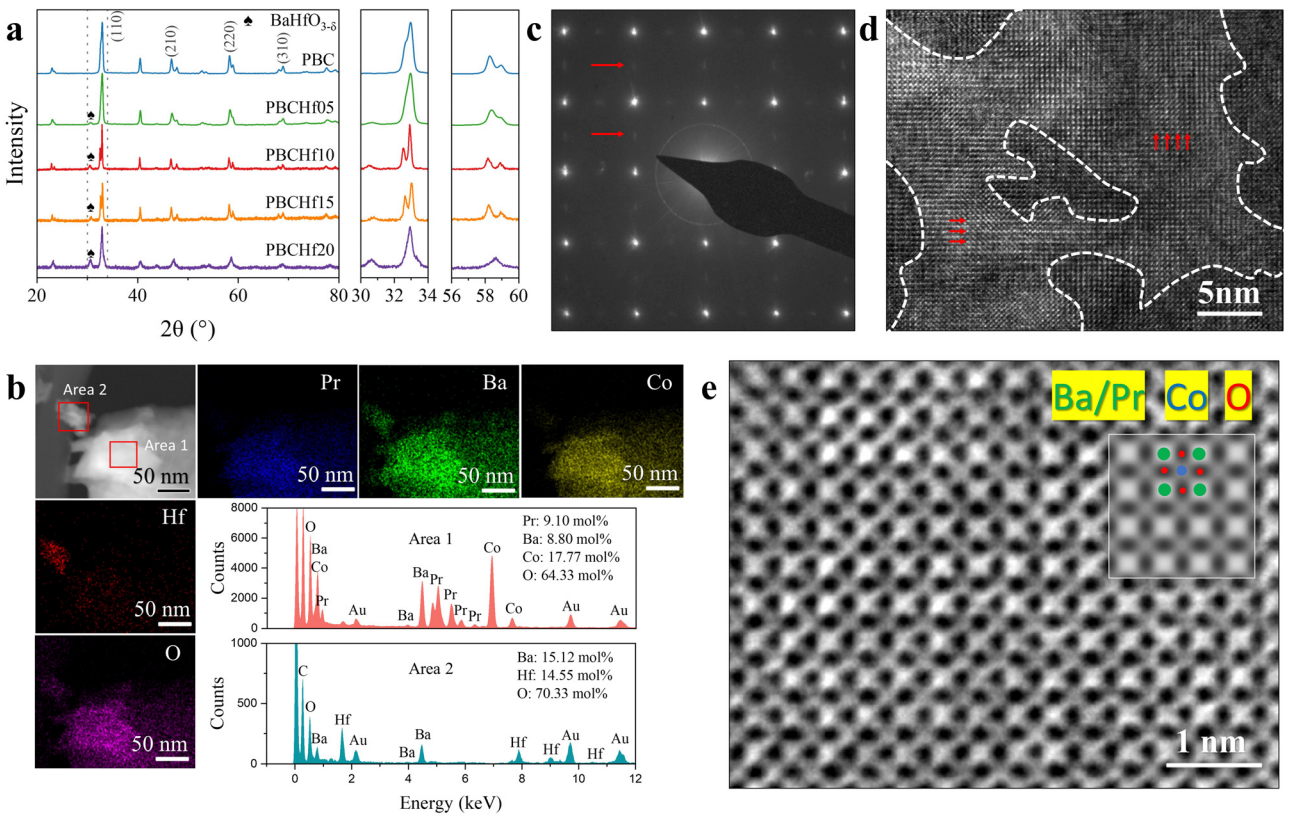

Fig. 3 Crystalline structure, chemical composition, microstructure and morphology of PBCHf10. (a) XRD patterns for PBC, PBCHf05, PBCHf10, PBCHf15 and PBCHf20. (b) TEM images of PBCHf10 powder accompanied by the corresponding EDS mapping. The EDS spectra for specific areas 1 and 2 are provided. (c) SAED pattern of PBCHf10, captured along the [100] zone axis, which is aligned parallel to the electron beam. Red arrows highlight the dimmer spots, indicating the presence of a secondary lattice structure, suggesting the existence of a double perovskite structure. (d) HRTEM image of PBCHf10. The white dashed line delineates the boundary between the brighter region and the darker region. Red arrows point to brighter regions, indicating the distribution of elements associated with the double perovskite structure. (e) HRTEM image showing a cross-section of PBCHf10 perpendicular to the (001) plane. Accompanying this image is a white block showing simulated results that correspond closely to the experimentally observed image.

This pattern clearly delineates the double perovskite structure in Pr-rich PBC, with brighter diffraction spots indicative of (100) plane reflections, while a secondary lattice, revealed through dimmer spots, corresponds to (200) plane reflections. The HRTEM images in Fig. 3d offer a detailed visualization of the atomic arrangement in these structures, confirming the prevalence of the double perovskite structure in brighter regions and the existence of a simple perovskite structure in darker regions. Furthermore, the lattice parameters measured at 3.91 Å from HRTEM images, observed perpendicular to the (001) plane (as shown in Fig. 3e), align with the values acquired from Rietveld refinement of the XRD spectra (3.90 Å), further substantiating the structural interpretation.

Experimental assessment of the electro-catalytic activity

A composite electrode composed of Pr-rich PBC and BHO displayed exceptionally high activity for the oxygen reduction reaction (ORR), evidenced by the remarkably low polarization resistance (R_p) and activation energy (0.95 eV) below 600 °C as determined in a symmetrical cell using Sm-doped ceria (SDC) as the electrolyte and PBCHf10 as the electrodes (Fig. S15–S19, ESI†). The outstanding electro-catalytic activity of PBCHf10 is attributed to the presence of the PBC–BHO interface, which effectively accelerates the rate-determining step (oxygen dissociation process) in the ORR (Fig. S20, ESI†). To confirm PBCHf10's outstanding ORR activities at low temperatures, the impedance of a symmetrical cell based on a proton conducting electrolyte, PBCHf10/BZCYYb1711/PBCHf10, was acquired in wet air (~3% water vapor) to determine the resistance to the ORR, R_p. At 700, 650, 600, 550, and 500 °C, the estimated R_p values are, respectively, 0.044, 0.089, 0.187, 0.374, and 0.933 Ω cm^2 (Fig. S21, ESI†) with an E_a of 0.98 eV. These results underscore its exceptional ORR activity compared with that of the pristine PBC and state-of-the-art materials, as detailed in Fig. S22 and S23 (ESI†).[5,32–40] Interestingly, as demonstrated in Fig. S24 (ESI†), the R_p progressively decreased with increasing water vapor pressure (P_{H_2O}), dropping from 0.224 to 0.187 Ω cm^2 at 600 °C upon the introduction of 3% P_{H_2O} and further reducing to 0.149 and 0.123 Ω cm^2 with 10% and 30% P_{H_2O}, respectively. The distribution of relaxation time (DRT) analysis of the impedance data (Fig. S25, ESI†) revealed a marked decrease in the low and medium frequency peaks with rising P_{H_2O}. This novel ORR/OER behavior in a proton-conducting system suggests a distinct reaction mechanism that is intricately linked to the presence of water. The observed decrease in impedance of the rate-determining steps with the increase in water vapor pressure has motivated us to conduct more in-depth investigations.

X-ray photoelectron spectroscopy (XPS) analyses of O 1s spectra were conducted for PBC, BHO, and PBCHf10, elucidating the information of oxygen-containing species present on their surface, as illustrated in Fig. S26 (ESI†). A notable finding was the variation in the hydroxide-to-lattice oxygen ratio ($R_{OH\text{-}Latt}$), with PBC displaying a ratio of 0.94, indicating higher surface hydration properties, compared to BHO's lower ratio of 0.36. These results align with our DFT calculations, which showed a higher surface hydration energy for PBC (−1.70 eV) than for BHO (−1.02 eV) (Fig. S27 and S28, ESI†). PBCHf10 demonstrated a similar $R_{OH\text{-}Latt}$ of 0.97, highlighting its superior surface hydration, due mainly to its primary phase, Pr-rich PBC. Furthermore, thermogravimetric analysis (TGA) revealed distinctly different behaviors between PBC and BHO (Fig. S29, ESI†). At 600 °C, PBC exhibited a weight loss of 0.71 wt%, indicative of significant oxygen vacancy concentration, as opposed to BHO's marginal weight loss of 0.16 wt%. This is consistent with our findings of vacancy formation energies, 3.53 eV for PBC and 6.46 eV for BHO, suggesting easier vacancy formation in PBC (Fig. S30 and S31, ESI†). When examining bulk hydration reactions, PBC showed a minimal weight increase at 600 °C (0.00043 wt%), implying restricted hydration capabilities. In contrast, BHO displays a substantial weight gain of 0.07 wt%, evidencing effective bulk hydration, with approximately 40% of its oxygen vacancies contributing to the hydration process under 3% water vapor pressure (Fig. S32, ESI†). This efficiency is comparable to a third of that observed in the well-known electrolyte BZCYYb1711.[12] We further investigated the protonic conductivity of PBC and BHO using *ab initio* molecular dynamics (AIMD) simulations. At 600 °C, BHO exhibits a diffusion coefficient (D_H) of 3.10 E^{-5} cm^2 s^{-1}, significantly higher than PBC's 7.62 E^{-6} cm^2 s^{-1}, as shown in Fig. S33–S36 (ESI†). This thorough analysis, incorporating both experimental and computational approaches, accentuates the distinct hydration characteristics of the two materials: PBC stands out for its exceptional surface hydration, enhancing the presence of surface hydroxides, while BHO demonstrates superior bulk hydration and protonic diffusion capabilities.

Considering the distinctive hydration properties of PBCHf10 and its remarkable water-induced enhancement in ORR activity, we propose a novel proton-involved ORR (PI-ORR) mechanism, which is distinctly different from the conventional ORR in a cell based on an oxygen ion conductor without the participation of protons. Fig. 4a schematically illustrates the elementary steps that may be involved in the ORR and PI-ORR on the PBC surface or the PBC–BHO interface. Both the ORR and PI-ORR encompass the same initial elementary steps, the adsorption and dissociation of molecular oxygen. The process begins with an inherent oxygen vacancy on the surface $\left(V_{O,surf}^{\bullet\bullet}\right)$, which creates an unsaturated environment conducive to the adsorption of oxygen molecule ($O_{2,gas}$), leading to the formation of superoxide species, denoted as $^*\left(O_I^{q_I}\ldots O_{II}^{q_{II}}\right)$,

$$V_{O,surf}^{\bullet\bullet} + O_{2,gas} + q_{ads}e' \rightarrow {}^*(O_I^{q_I}\ldots O_{II}^{q_{II}}) \quad (1)$$

This is quantified by an adsorption energy of −0.237 eV on the BO_2-terminated (001) PBC surface (Fig. 4b). Bader charge analysis reveals charges of q_I = 0.32 e and q_{II} = 0.48 e, for the involved oxygen atoms, O_I and O_{II}, as illustrated in Fig. S37 (ESI†). The PBC–BHO interface on the same plane shows improved oxygen adsorption properties, with an increased adsorption energy of −0.427 eV (Fig. 4c). A comparative charge distribution difference analysis for the PBC surface and the PBC–BHO interface with superoxide species underscores the enhanced oxygen–cobalt hybridization at the PBC–BHO interface (Fig. S38, ESI†). Following adsorption, the dissociation

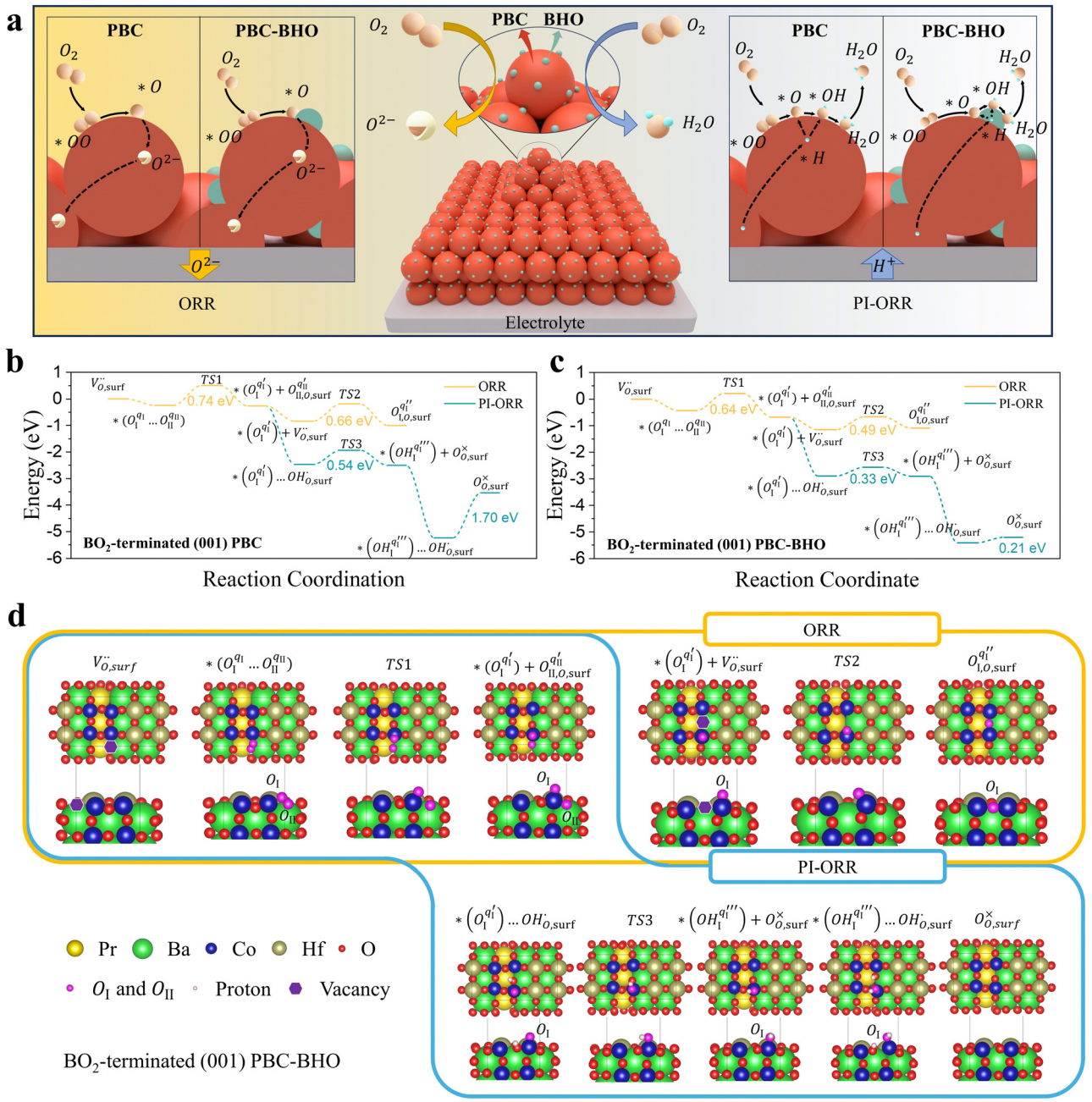

Fig. 4 Investigation of the electro-catalytic mechanism in PBCHf10. (a) Schematic representations of the ORR and PI-ORR on the PBC surface or the PBC–BHO interface. For clarity, chemical species are denoted as follows: 'O_2' for gas-phase oxygen, '*OO' for superoxide species, '*O' for peroxide species, 'O^{2-}' for oxygen ions, '*H' for protons, '*OH' for hydroxide species, and 'H_2O' for gas-phase water molecules. (b) and (c) Comparative analysis of the energy profiles for the ORR and PI-ORR on the BO_2-terminated (001) PBC surface (b) and the PBC–BHO interface (c). (d) Top and side views of the configurations during the ORR and PI-ORR on the BO_2-terminated (001) PBC–BHO interface.

reaction occurs,

$$^{*}\left(\mathrm{O_I^{q_I}}\ldots\mathrm{O_{II}^{q_{II}}}\right)+q_{\mathrm{diss}}\mathrm{e}'\rightarrow{}^{*}\left(\mathrm{O_I^{q_I'}}\right)+\mathrm{O_{II,O,surf}^{q_{II}'}}\qquad(2)$$

Here, the O_{II} combines with the vacancy site, becoming a surface-located lattice oxygen $O_{II,O,surf}^{q_{II}'}$. The remaining oxygen atom O_I is now identified as a peroxide species $^{*}\left(O_I^{q_I'}\right)$. The E_a for the PBC surface is calculated to be 0.74 eV, while the E_a for the PBC–BHO interface is dramatically reduced to 0.64 eV. The difference between the two mechanisms arises from the consumption of peroxide. In the ORR, the process involves the transportation of O_{II}, the incorporation of O_I, and the regeneration of new oxygen vacancies on the surface (detailed in the ESI†). In the PI-ORR, by contrast, an additional pathway is facilitated by the surface protons $\left(OH_{O,surf}^{\bullet}\right)$ originated, sourced from either PBC or BHO, enabling the first

hydrogenation of the peroxide species, leading to the formation of hydroxide species $^{*}\left(\mathrm{OH}_{\mathrm{I}}^{q'''_{\mathrm{I}}}\right)$,

$$^{*}\left(\mathrm{O}_{\mathrm{I}}^{q'_{\mathrm{I}}}\right)\ldots\mathrm{OH}_{\mathrm{O,surf}}^{\bullet}+q_{\mathrm{hydro1}}\mathrm{e}'\rightarrow{}^{*}\left(\mathrm{OH}_{\mathrm{I}}^{q'''_{\mathrm{I}}}\right)+\mathrm{O}_{\mathrm{O,surf}}^{\times}\qquad(3)$$

For the PBC surface, the E_a required for the first hydrogenation is found to be 0.54 eV, which is notably lower than the 0.66 eV required for the conventional incorporation reaction. For the PBC–BHO interface, this energy is further reduced to 0.33 eV; the dramatic reduction in this energy barrier results in its exceptional performance. The subsequent second hydrogenation reaction leads to the formation and desorption of water molecules, regenerating a clean surface,

$$^{*}\left(\mathrm{OH}_{\mathrm{I}}^{q'''_{\mathrm{I}}}\right)\ldots\mathrm{OH}_{\mathrm{O,surf}}^{\bullet}+q_{\mathrm{hydro2}}\mathrm{e}'\rightarrow\mathrm{H_2O_{gas}}+\mathrm{O}_{\mathrm{O,surf}}^{\times}\qquad(4)$$

A relatively high water desorption energy of 1.70 eV is found for the PBC surface, posing a significant challenge that can disrupt the continuity of the entire PI-ORR process due to inefficient water desorption. However, the PBC–BHO interface substantially improves this, showcasing a drastically lower water desorption energy of 0.21 eV, as further confirmed by XPS results in Fig. S26 (ESI†). This enhancement is critical for sustaining the entire PI-ORR process, as evidenced by the detailed configurations presented in Fig. 4d and Fig. S39 (ESI†).

Experimental assessment of the thermodynamic stability

To assess the phase stability, *in situ* high-temperature XRD tests were performed under both dry and wet air, as shown in Fig. S40 (ESI†), revealing that the crystal structure of PBCHf10 is stable from 50 to 700 °C. However, a notable shift in the primary peak indicates a lattice expansion with temperature. Subsequent Rietveld refinement analysis confirms consistent lattice parameters for Pr-rich PBC and BHO under the experimental conditions studied (Fig. S41 and Table S3, ESI†). This consistency underscores the exceptional structural stability of Pr-rich PBC and BHO composite electrodes under the testing conditions. Hence, to further validate its thermodynamic stability, a long-term durability test was conducted in wet air with 30% water vapor pressure at 600 °C for 500 hours (Fig. S42, ESI†). To assess the durability of the PBCHf10 electrode when exposed to a high P_{H_2O}, SEM images were taken of cells before and after the durability testing (Fig. S43, ESI†). The analysis of grain size and distribution reveals that the microstructure and the morphology of both components of the composite electrode remained intact. This finding was corroborated by similar durability tests conducted on a strip sample, where the crystal surface of Pr-rich PBC showed no discernible changes, and there was no observable growth in the size of the BHO phase (Fig. S44, ESI†). Furthermore, XRD examination of the electrodes after durability tests (Fig. S45, ESI†) did not find any additional peaks, further confirming PBCHf10's thermodynamic stability under the tested conditions. These durability assessments underscore PBCHf10's robustness and suitability for practical applications in PCECs, demonstrating the effectiveness of our material screening strategy that integrates the E_{hull} theory with the DA method.

Verification in PCECs

Given PBCHf10's exceptional electro-catalytic activity and remarkable durability even under a high P_{H_2O}, we also tested it as the oxygen electrode in PCECs. Prior to this, its physicochemical properties as an oxygen electrode were thoroughly analyzed (Fig. S46–S52, ESI†). Fig. 5a shows a cross-sectional SEM image of a single PCEC, revealing a seamless integration of the PBCHf10 electrode with the BSCYb172 electrolyte. The open circuit voltages (OCVs) were 1.12, 1.11, 1.09 and 1.08 V at 450, 500, 550, and 600 °C, respectively, demonstrating the effective electron blocking capabilities of the BSCYb172 electrolyte. Impedance data acquired at OCV (Fig. 5b and c) revealed that the ohmic resistance (R_o) and the R_p at 600 °C were 0.069 and 0.070 Ω cm^2, respectively, emphasizing the superior protonic conductivity of BSCYb172 and the exceptional electro-catalytic activity of PBCHf10. In the fuel cell mode, peak power densities of 1.49, 1.29, 0.93, and 0.60 W cm^{-2} are demonstrated at 600 to 450 °C (Fig. 5d), which are among the best reported in the literature (Fig. 5e and detailed in Table S4, ESI†).[1,2,5,12,24,32–42] It is particularly worthy to note that the peak power density (PPD) demonstrated at 450 °C and 0.60 W cm^{-2} is ∼9% higher than the highest PPD previously reported at this temperature (0.55 W cm^{-2}), achieved with an ultrathin (3 μm) electrolyte fabricated by an ultrasonic spray-coating technique.[2] In contrast, our PCEC with a 7 μm electrolyte was fabricated using a low-cost conventional process. This achievement highlights the exceptional PI-ORR activity of PBCHf10 at reduced temperatures, offering the potential to dramatically reduce the cost of PCEC technology. This is because it allows the use of much less expensive materials in other components of PCEC systems when operating at these reduced temperatures.

The outstanding performance and remarkable durability of the symmetric cells in wet air with a P_{H_2O} of 30%, as previously discussed, inspired us to further investigate the system by increasing the P_{H_2O} at the oxygen electrode and examining its performance under electrolysis mode. Accordingly, we conducted electrolysis tests in wet air with a P_{H_2O} of 30% at different temperatures; the results are presented in Fig. 5f. The current densities at an applied cell voltage of 1.3 V were 2.78, 1.98, 0.89, 0.4, and 0.16 A cm^{-2} at 600, 550, 500, 450, and 400 °C, respectively. These results highlight the system's exceptional performance when compared to those reported previously (Fig. S53 and Table S5, ESI†).[5,12,24,32–42] A detailed computational analysis is presented in Fig. S54 and Table S6 (ESI†).

Furthermore, the PCEC was operated in a galvanostatic mode for a longer period of continuous operation to assess the system's durability. In the fuel cell mode at 600 °C, little variation in cell voltage for ∼200 hours at a current density of 0.3 A cm^{-2} (Fig. 5g) implies reasonable stability. In the electrolysis mode, the cell voltage remained relatively stable for ∼500 hours at a constant current density of −0.5 A cm^2 when the oxygen electrode was exposed to wet air with a P_{H_2O} of 3%

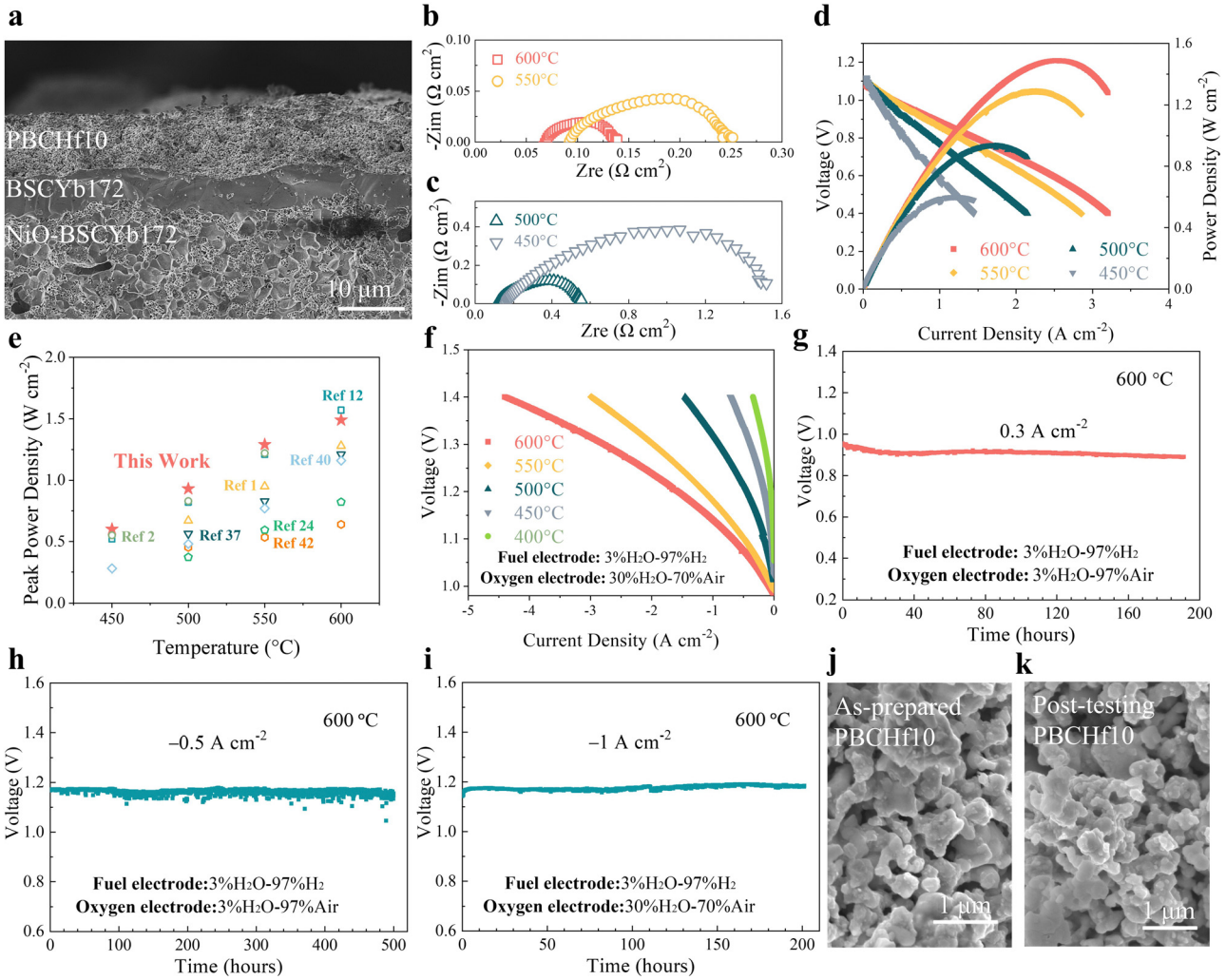

Fig. 5 Electrochemical performance and long-term durability performance of a PBCHf10 single cell. (a) Cross-sectional SEM image showcasing the architecture of a PBCHf10/BSCYb172/Ni-BSCYb172 single cell. (b) and (c) EIS results for the single cell under OCV conditions at 600–450 °C. (d) Typical *I*–*V*–*P* curves measured at 600–450 °C, with H_2 (3% water vapor pressure) at the fuel electrode and air at the oxygen electrode. (e) Comparative analysis of peak power densities for PCECs at 700–450 °C. (f) Typical *I*–*V* curves recorded in the electrolysis mode at 600–400 °C, with H_2 (3% water vapor pressure) at the fuel electrode and air (30% water vapor pressure) at the oxygen electrode. (g)–(i) Long-term galvanostatic tests of the PBCHf10/BSCYb172/NiO-BSCYb172 single cell at 600 °C under the (g) fuel cell mode at a current density of 0.3 A cm^{-2}, (h) electrolysis mode at a current density of −0.5 A cm^{-2}, incorporating humidity of 3% water vapor pressure in the oxygen electrode, and (i) electrolysis mode at a higher current density of −1 A cm^{-2}, with increased humidity of 30% water vapor pressure in the oxygen electrode. (j) and (k) Cross-sectional SEM images of the (j) as-prepared oxygen electrode, and (k) oxygen electrode post long-term durability testing, specifically following the test shown in (i).

(Fig. 5h). Additionally, the cell was tested under more stringent conditions for water electrolysis by increasing the current density to −1 A cm^2 and the P_{H_2O} to 30% in the oxygen electrode compartment. During the 200-hour durability test under this condition (Fig. 5i), the cell voltage increased slightly, from 1.171 to 1.184 V, implying excellent durability. Examination of cross-sectional SEM images (Fig. S55, ESI†) revealed that the morphology of the oxygen electrode remained relatively constant during the 200 hour operation. The oxygen electrode's surface (Fig. 5j and k) exhibited no notable changes, affirming the superior stability of PBCHf10. Furthermore, the system cycling stability was demonstrated under alternating fuel cell and electrolysis modes at 600 °C, as highlighted in Fig. S56 (ESI†), switching modes every two hours at current densities of ±0.3 A cm^{-2}.

Conclusions

Through the integration of high-throughput calculations and computational chemistry databases, our study has successfully evaluated the thermodynamic stability and decomposition tendencies of an unprecedented dataset of 4455 distinct perovskite oxide candidates. This data-driven high-throughput calculation approach, combined with a novel decomposition analysis method, not only addresses the limitations of the E_{hull} theory, enabling the accurate determination of materials' true thermodynamic stability, but also enhances the forecasting of composite structures. From our calculated database, we discovered a groundbreaking oxygen electrode, $PrBaCo_{1.9}Hf_{0.1}O_{5+\delta}$, for PCECs, validated through comprehensive experimental investigations and

detailed computational simulations to exhibit superior electrocatalytic activity and durability. The study further reveals intricate mechanisms behind oxygen reduction reactions with or without the participation of protons, offering valuable insights for the rational design of perovskite oxide electrodes in a broader chemical space for PCECs. Furthermore, the data-driven high-throughput calculation methodology is applicable for expediting material screening processes vital for the advancement of other energy storage and conversion technologies, including batteries, supercapacitors, and solar cells.

Author contributions

X. H., Y. Z., Z. L., H. L., and M. L. conceived the ideas for this study and designed the experiments. X. H. conducted high-throughput DFT calculations. X. H. designed the decomposition analysis method and conducted detailed DFT calculations and MD simulations. Y. Z. and Z. L. performed the fabrication and testing experiments of PCEC single cells. X. H. synthesized and tested the oxygen electrode materials. H. L. performed XPS. N. S. performed *in situ* XRD, TG, and TEC analyses. Z. L., W. Z., and W. W. performed XRD and SEM. Y. D. performed TEM. X. H., Z. L., H. L., and M. L. wrote the manuscript. All authors have discussed and approved the final manuscript.

Data availability

The data supporting this article have been included as part of the ESI.† The code for high-throughput calculations and decomposition analysis can be obtained from **https://github.com/XueyuHu/HighthroughputCalculation**.

Conflicts of interest

There are no conflicts to declare.

Acknowledgements

This work was supported by the U.S. Department of Energy (Award Number DE-FE0031975), Phillips 66, and the Hightower Endowment to the Georgia Tech Foundation.

Notes and references

1 Z. Wang, Y. H. Wang, J. Wang, Y. F. Song, M. J. Robson, A. Seong, M. T. Yang, Z. Q. Zhang, A. Belotti, J. P. Liu, G. Kim, J. Lim, Z. P. Shao and F. Ciucci, *Nat. Catal.*, 2022, **5**, 777–787.
2 F. Liu, H. Deng, D. Diercks, P. Kumar, M. H. A. Jabbar, C. Gumeci, Y. Furuya, N. Dale, T. Oku, M. Usuda, P. Kazempoor, L. Y. Fang, D. Chen, B. Liu and C. C. Duan, *Nat. Energy*, 2023, **8**, 1145–1157.
3 W. J. Bian, W. Wu, B. M. Wang, W. Tang, M. Zhou, C. R. Jin, H. P. Ding, W. W. Fan, Y. H. Dong, J. Li and D. Ding, *Nature*, 2022, **604**, 479.
4 M. Li, B. Hua, L. C. Wang, J. D. Sugar, W. Wu, Y. Ding, J. Li and D. Ding, *Nat. Catal.*, 2021, **4**, 274–283.
5 Y. C. Zhou, E. Z. Liu, Y. Chen, Y. C. Liu, L. Zhang, W. L. Zhang, Z. Y. Luo, N. Kane, B. Zhao, L. Soule, Y. H. Niu, Y. Ding, H. P. Ding, D. Ding and M. L. Liu, *ACS Energy Lett.*, 2021, **6**, 1511–1520.
6 J. Cao, Y. Ji and Z. Shao, *Chem. Soc. Rev.*, 2024, **53**, 450–501.
7 S. Choi, C. J. Kucharczyk, Y. G. Liang, X. H. Zhang, I. Takeuchi, H. I. Ji and S. M. Haile, *Nat. Energy*, 2018, **3**, 202–210.
8 Z. C. Zhuang, Y. H. Li, R. H. Yu, L. X. Xia, J. R. Yang, Z. Q. Lang, J. X. Zhu, J. Z. Huang, J. O. Wang, Y. Wang, L. D. Fan, J. S. Wu, Y. Zhao, D. S. Wang and Y. D. Li, *Nat. Catal.*, 2022, **5**, 300–310.
9 M. Zhong, K. Tran, Y. M. Min, C. H. Wang, Z. Y. Wang, C. T. Dinh, P. De Luna, Z. Q. Yu, A. S. Rasouli, P. Brodersen, S. Sun, O. Voznyy, C. S. Tan, M. Askerka, F. L. Che, M. Liu, A. Seifitokaldani, Y. J. Pang, S. C. Lo, A. Ip, Z. Ulissi and E. H. Sargent, *Nature*, 2020, **581**, 178.
10 R. Jacobs, T. Mayeshiba, J. Booske and D. Morgan, *Adv. Energy Mater.*, 2018, **8**, 1702708.
11 S. Fujii, Y. Shimizu, J. Hyodo, A. Kuwabara and Y. Yamazaki, *Adv. Energy Mater.*, 2023, **13**, 2301892.
12 Z. Luo, X. Hu, Y. Zhou, Y. Ding, W. Zhang, T. Li and M. Liu, *Adv. Mater.*, 2024, 2311159.
13 J. Y. Peng, D. Schwalbe-Koda, K. Akkiraju, T. Xie, L. Giordano, Y. Yu, C. J. Eom, J. R. Lunger, D. J. Zheng, R. R. Rao, S. Muy, J. C. Grossman, K. Reuter, R. Gómez-Bombarelli and Y. Shao-Horn, *Nat. Rev. Mater.*, 2022, **7**, 991–1009.
14 S. Zhai, H. P. Xie, P. Cui, D. Q. Guan, J. Wang, S. Y. Zhao, B. Chen, Y. F. Song, Z. P. Shao and M. Ni, *Nat. Energy*, 2022, **7**, 866–875.
15 N. Wang, B. Y. Yuan, C. M. Tang, L. Du, R. J. Zhu, Y. Aoki, W. B. Wang, L. X. Xing and S. Y. Ye, *Adv. Mater.*, 2022, **34**, 2309855.
16 I. T. Bello, R. Taiwo, O. C. Esan, A. H. Adegoke, A. O. Ijaola, Z. Li, S. Y. Zhao, C. Wang, Z. P. Shao and M. Ni, *Energy AI*, 2024, **15**, 100317.
17 C. Chen, Y. X. Zuo, W. K. Ye, X. G. Li, Z. Deng and S. P. Ong, *Adv. Energy Mater.*, 2020, **10**, 1903242.
18 A. Merchant, S. Batzner, S. S. Schoenholz, M. Aykol, G. Cheon and E. D. Cubuk, *Nature*, 2023, 1–6.
19 A. Jain, S. P. Ong, G. Hautier, W. Chen, W. D. Richards, S. Dacek, S. Cholia, D. Gunter, D. Skinner, G. Ceder and K. A. Persson, *APL Mater.*, 2013, **1**, 011002.
20 S. J. Skinner, *Int. J. Inorg. Mater.*, 2001, **3**, 113–121.
21 Z. P. Shao and S. M. Haile, *Nature*, 2004, **431**, 170–173.
22 C. R. Xia, W. Rauch, F. L. Chen and M. L. Liu, *Solid State Ionics*, 2002, **149**, 11–19.
23 C. C. Duan, J. H. Tong, M. Shang, S. Nikodemski, M. Sanders, S. Ricote, A. Almansoori and R. O'Hayre, *Science*, 2015, **349**, 1321–1326.
24 S. Choi, T. C. Davenport and S. M. Haile, *Energy Environ. Sci.*, 2019, **12**, 206–215.
25 V. Somjit and B. Yildiz, *ACS Appl. Mater. Interfaces*, 2022, **14**, 42613–42627.

26 C. Chen and S. P. Ong, *Nat. Comput. Sci.*, 2022, **2**, 718.
27 J. H. Kim, D. Kim, S. Ahn, K. J. Kim, S. Jeon, D.-K. Lim, J. K. Kim, U. Kim, H.-N. Im and B. Koo, *Energy Environ. Sci.*, 2023, **16**, 3803–3814.
28 M. Li, M. Zhao, F. Li, W. Zhou, V. K. Peterson, X. Xu, Z. Shao, I. Gentle and Z. Zhu, *Nat. Commun.*, 2017, **8**, 13990.
29 X. Y. Hu, Y. Xie, Y. H. Wan, Y. Yang, X. J. Wu and C. R. Xia, *Appl. Catal., B*, 2021, **286**, 119901.
30 X. Mao, Z. H. Li, M. R. Li, X. Y. Xu, C. Yan, Z. H. Zhu and A. J. Du, *J. Am. Chem. Soc.*, 2021, **143**, 9507–9514.
31 X. Y. Zhang, R. Song, D. M. Huan, K. Zhu, X. Y. Li, H. R. Han, C. R. Xia, R. R. Peng and Y. L. Lu, *Small*, 2022, **18**, 2205190.
32 H. P. Ding, W. Wu, C. Jiang, Y. Ding, W. J. Bian, B. X. Hu, P. Singh, C. J. Orme, L. C. Wang, Y. Y. Zhang and D. Ding, *Nat. Commun.*, 2020, **11**, 1907.
33 Z. Q. Liu, D. F. Cheng, Y. L. Zhu, M. Z. Liang, M. T. Yang, G. M. Yang, R. Ran, W. Wang, W. Zhou and Z. P. Shao, *Chem. Eng. J.*, 2022, **450**, 137787.
34 K. Pei, S. R. Luo, F. He, J. Arbiol, Y. S. Xu, F. Zhu, Y. K. Wang and Y. Chen, *Appl. Catal., B*, 2023, **330**, 122601.
35 M. Z. Liang, Y. H. Wang, Y. F. Song, D. Q. Guan, J. Wu, P. Chen, A. Maradesa, M. G. Xu, G. M. Yang, W. Zhou, W. Wang, R. Ran, F. Ciucci and Z. P. Sha, *Appl. Catal., B*, 2023, **331**, 122682.
36 Y. H. Niu, Y. C. Zhou, W. L. Zhang, Y. X. Zhang, C. Evans, Z. Y. Luo, N. Kane, Y. Ding, Y. Chen, X. Y. Guo, W. Q. Lv and M. L. Liu, *Adv. Energy Mater.*, 2022, **12**, 2103783.
37 K. Pei, Y. C. Zhou, K. Xu, H. Zhang, Y. Ding, B. T. Zhao, W. Yuan, K. Sasaki, Y. M. Choi, Y. Chen and M. L. Liu, *Nat. Commun.*, 2022, **13**, 2207.
38 F. He, Y. C. Zhou, T. Hu, Y. S. Xu, M. Y. Hou, F. Zhu, D. L. Liu, H. Zhang, K. Xu, M. L. Liu and Y. Chen, *Adv. Mater.*, 2023, **35**, 2209469.
39 F. He, S. Liu, T. Wu, M. T. Yang, W. H. Li, G. M. Yang, F. Zhu, H. Zhang, K. Pei, Y. Chen, W. Zhou and Z. P. Shao, *Adv. Funct. Mater.*, 2022, **32**, 2206756.
40 M. Saqib, I. G. Choi, H. Bae, K. Park, J. S. Shin, Y. D. Kim, J. I. Lee, M. Jo, Y. C. Kim, K. S. Lee, S. J. Song, E. D. Wachsman and J. Y. Park, *Energy Environ. Sci.*, 2021, **14**, 2472–2484.
41 W. Zhang, Y. Zhou, X. Hu, Y. Ding, J. Gao, Z. Luo, T. Li, N. Kane, X.-Y. Yu and T. Terlier, *ACS Energy Lett.*, 2023, **8**, 3999–4007.
42 C. C. Duan, R. Kee, H. Y. Zhu, N. Sullivan, L. Z. Zhu, L. Z. Bian, D. Jennings and R. O'Hayre, *Nat. Energy*, 2019, **4**, 230–240.